CHAPTER-4

Synthesis and characterizations of α-MnSe/ppy heterostructures as high-performance electrocatalysts for oxygen evolution reaction with *operando* mechanistic insights

4.1. Abstract

The extremely slow kinetics of the water-splitting process stymies the synthesis of hydrogen (H_2) from water. To comprehend the main obstacle to OER, it is also necessary to enhance the development of efficient OER electrocatalysts. In this work, manganese selenide with polypyrrole heterostructure is synthesized, described, and electrochemically assessed as an effective electrocatalyst for OER. The novel synthesized material is characterized using a variety of techniques, including scanning electron microscopy (SEM), powder x-ray diffraction (PXRD), transmission electron microscopy (TEM) etc. The unique α-MnSe/ppy composite catalyst is shown to be exceedingly efficient, starting the OER at an astoundingly low voltage of 168 mV (vs. reversible hydrogen electrode [RHE]) at 10 mA cm^{-2}, with a tafel slope of 67 mV dec^{-1}. Also, *operando* UV-Vis spectro-electrochemical studies give an insight towards the intermediate species formed during the OER catalysis. Under similar electrochemical conditions, the α-MnSe/ppy electrocatalyst outperforms its α-MnSe and ppy counterparts for OER in an aqueous KOH (1.0 M) solution. These results surpass benchmark electrocatalysts made of Mn and rare earth metals. With this invention, a desired non-noble metal is made available that works excellently as an OER electrocatalyst.

4.2. Introduction

In order to address the issues of the present environmental harm and energy crisis brought on by the excessive use of non-renewable energy, there has recently been a considerable focus on the generation of ecologically friendly and renewable energy supplies [1–4]. A great deal of interest has also been generated by developments in affordable and effective technology for a

variety of energy harvesting and gathering applications. In this context, OER and HER are two essential processes in the electrochemical splitting of water, which have caught the attention of researchers as good methods for producing sustainable energy sources like hydrogen fuels [5–8]. Although the proton-electron channel used in hydrogen production is simple, the counter OER is somewhat lengthy. Numerous proton-coupled electron transfer steps are present, which leads to low efficiency and a large overpotential. The OER is a crucial process in many energy storage devices, including metal-air batteries, in addition to water splitting [9–11]. Whilst a consequence, efficient electrocatalysts are highly recommended since they significantly contribute to speeding the reaction by lowering the overpotential and enhancing the kinetics of the sluggish reaction.

Among the most powerful electrocatalysts so far have been discovered to be those comprised of rare earths, such as iridium and ruthenium oxide, but their high expense, limited availability, and poor ability to store in alkaline environments severely restrict their widespread use [12]. Due to their low overpotentials and prolonged stability, a number of transition metal (TM) compounds and their derivatives, including chalcogenides, such as selenides, oxides, hydroxides/oxyhydroxides, nitrides, phosphides, have recently been produced for OER. Because of their varied electronic structure, superior electrocatalytic results, and enduring stability, TM chalcogenides among other materials provide better OER outcomes and may also function as an appealing option for OER electrocatalyst [13–16]. However, it has long been recognized that certain crystal systems of the TM chalcogenides possess noteworthy electrical and magnetic characteristics. The electrical structure and framework of these TM chalcogenide electrode substrates are expected to be significantly altered by ion exchange, which will allow

researchers to adjust various electrode material properties during the water oxidation process [17–20]. Additionally, changes in the metal-to-chalcogen ratio may have a significant effect on the electrical properties of electrode materials.

Manganese sulfide, one of the numerous kinds of TM chalcogenides, is a polymorphic mineral that may be found in a variety of phases, including wurtzite (γ-MnS), rock salt (α-MnS), zinc-blende (β-MnS), and cubic (MnS_2) [21]. As they closely related, equivalent of MnS, manganese selenide (MnSe) is a p-type semiconductor with a band gap of 2.0 eV [22]. MnSe may thus crystallize into three different types of structural forms just like MnS, including wurtzite (WZ) [23,24], zinc blende (ZB) [25], and rock salt (RS) [26,27]. Among these, rock salt MnSe (α-MnSe) is a stable phase, and a significant amount of pertinent studies have traditionally concentrated on its magnetic and optical characteristics, with just a few investigations focusing on its electrochemical performance [28].

Conducting polymers are frequently utilized to immobilize the scattered metal catalysts. Because of their large surface area and porous nature, conducting polymers are preferred as an auxiliary material in the development of new electrocatalysts. The polymer chains' relatively high electrical conductivity aids in moving the electrons in an electrocatalytic process between the electrodes and dispersed metal particles. Thus, these composite materials are capable of producing the efficient electrocatalysts. The use of conducting polymers as secondary matrices as catalytically efficient particles for the immobilization has received enough attention [29]. Conducting polymers may be employed as the electrode material for supercapacitors due to their adjustable electrical conductivity and redox states. Polypyrrole (ppy), one of the conducting polymers, has drawn the most attention because of its improved

redox behavior, environmental stability, high conductivity, and commercial availability of starting monomers [30].

Recently researchers are focused on transition metal chalcogenides in the field of electrochemical water splitting. Alharbi *et al.* prepared nanosized manganese based chalcogenide composite (MnS/MnO) for enhanced electrocatalytic OER [31]. Tigwere *et al.* doped the MnS nanostructure with different transition metals such as Fe, Cu and Ni for enhancing the water splitting activity and supercapacitance [32]. A lot of work based on manganese chalcogenides [33] has been done but none of them mention the manganese selenide and its different phases. This might be due to its poor performance towards OER than other selenide materials. To improve the efficiency of α-MnSe as an effective electrocatalyst in water splitting applications, we concentrated on merging the material with conducting polymer (ppy) and obtained greater efficiency of α-MnSe in an environment of polymer composite.

In the present study, we develop a novel α-MnSe/ppy electrocatalyst as an electrode material for OER using the hydrothermal technique, and we use a variety of analytical methods to look at the electrocatalyst's intrinsic properties. The physical findings support the development of the hybrids with various morphologies. According to the OER results, α-MnSe/ppy has the highest durability in 1.0 M aqueous potassium hydroxide electrolyte and the lowest overpotential at 10 mA cm^{-2}. This finding highlights the value of widely accessible, readily available electrocatalysts discovered and offers the chance for further research into the performance of OER electrocatalysts.

4.3. Experimental

4.3.1. Materials

Manganese Chloride hexahydrate ($MnCl_2 \cdot 6H_2O$) (AR, Merck, 99.9%), Selenium powder (AR, Merck, 99.9%), Hydrazine hydrate ($N_2H_4.xH_2O$), (AR, Merck, 99.9%), Pyrrole (AR, Merck, 99.9%).

4.3.2. Synthesis of α-MnSe

The proposed α-MnSe was prepared by using hydrothermal method. In this typical synthesis method, the stoichiometric amount of manganese chloride hexahydrate (1.1 mmol) was dissolved in 20 mL of water followed by stirring under vigorous conditions for 15 min. After that, about 0.11 g of Se powder was added to the above solution and stirring continued up to 30 min. To that mixture solution, 10 mL of $N_2H_4 \cdot xH_2O$ was added dropwise to form a black precipitate. Then, the whole solution was kept under magnetic stirring for 2 h. Finally, the black precipitate was transferred into the 50 mL Teflon equipped autoclave and kept at 180 ºC for 12 h in a hot air oven. After the reaction, the mixture solution was allowed to cool at room temperature. Then, the obtained precipitate was washed several times with water/ethanol and dried overnight at 45 ºC.

4.3.3. Synthesis of polypyrrole

The pyrrole monomer was stored under an inert atmosphere to prevent oxidation. 0.4 mL of pyrrole monomer was dispersed in 50 mL of distilled water and allowed to stirred completely for complete dispersion. Then, 50 mL of aqueous solution of anhydrous ferric chloride was

dropwise added to the mixture with continuous stirring in a N_2 atmosphere. The polymerization mixture was held at temperature of 0–5 ^oC for 6 h. Finally, the obtained polypyrrole was filtered and washed with distilled water and methanol to a neutral pH and dried at 60 ^oC under vacuum for 12 h.

4.3.4. Synthesis of α-MnSe/ppy composite

The composite material is formed by solid state method. The equal amounts of prepared α-MnSe and polypyrrole were taken in a mortar pestle for grinding about 2 to 3 hrs followed by ultrasonication in ethanol solution of the same for about an hour. The prepared composite material is then dried at 45 ^oC.

4.3.5. Preparation of working electrode

Fluorine doped tin oxide (FTO) was used as a support for the working electrode. To make the catalyst ink, 1 mg of the prepared catalyst was dispersed in a solution of 20 μL Nafion (5%) and 40 μL ethyl alcohol, and then ultrasonicated for about an hour. About 20 μL of prepared catalyst ink was then dropwise-casted with the smallest drop followed by drying at room temperature.

4.3.6. Electrode preparation for spectro-electrochemical study

The obtained ink from the aforementioned method is used to prepare the working electrode for the *operando* spectro-electrochemical study. By immersing the platinum grid in the catalyst ink and then drying it at room temperature, the platinum grid is made ready to be used as a working electrode.

4.4. Characterizations

4.4.1. Physicochemical characterizations

With a wavelength of 1.514 A°, powder X-ray diffraction (XRD) on a Rigaku Smart Lab 9 kW powder type was used to analyze the crystalline and amorphous nature of the prepared samples. The materials' morphologies and microstructures were determined using Thermo Fisher Technai 20 G^2 for HR-TEM and Nova Nano-SEM for field emission-scanning electron microscopy (FE-SEM). The elemental composition and their relative abundance have been analyzed by EDS and elemental mapping.

4.4.2. Electrochemical characterizations

Electrochemical analyses were conducted using a three-electrode setup in a single compartment Pyrex glass cell. The counter electrode consisted of a Pt foil (Aldrich 99.9% pure) with an area of 8 cm^2, while the working electrode was made of FTO/catalyst with a working surface area of 0.5 cm^2. A reference electrode of Hg/HgO/1M KOH was utilized, with all potentials referenced to its standard potential ($E^0_{Hg/HgO}$) of 105.3 mV vs. NHE [34]. A Luggin capillary salt bridge, prepared using agar-agar and KCl, was employed to connect the cell electrolyte to the reference electrode. Electrochemical characterizations, including cyclic voltammetry, impedance measurements, and Tafel polarization investigations [35–37], were carried out using a CHI-608C instrument (CH instrument, USA). To relate potential values measured by the Hg/HgO reference electrode to the reversible hydrogen electrode (RHE), **Equation 3.1** could be used which is already discussed in **Chapter 3**.

$$E_{RHE} = E_{Hg/HgO} + 0.0592 \times pH + E^{0}_{Hg/HgO} \quad \textbf{(3.1)}$$

4.4.3. Spectro-electrochemical characterizations

During spectro-electrochemical investigations, within a quartz cuvette, the catalyst ink-immersed platinum grid functioned as the working electrode, while a platinum wire served as the counter electrode. The reference electrode comprised Hg/HgO in 1 M KOH solution. A luggin capillary salt bridge, composed of agar-agar and KCl, facilitated connection between the reference electrode and the cell electrolyte. Cyclic voltammetry was performed at a scan rate of 20 mV s^{-1}, with spectra recorded closest to the onset potential. *Operando* spectro-electrochemical analyses were conducted using the Ocean Optics FLAME-T-XR1-ES Assembly covering a wavelength range of 200 nm to 1025 nm.

4.5. Results and discussion

4.5.1. Physicochemical characterizations

4.5.1.1. XRD

The XRD patterns of composite including polymer (ppy) and α-MnSe powders are shown in **Figure 4.1**. The XRD patterns' wide peaks attest to ppy's amorphous character. These patterns closely resemble those that have already been documented [38], [35]. All peaks are indexed with pyrite structured α-MnSe, is shown by comparing the reflections with JCPDS card no. 11-0683 and finding that all basic reflections (h, k, l = all even or odd) are present. The composite exhibits a coexistence of crystalline and amorphous phases with some additional

peaks of other phases i.e., β-MnSe and γ-MnSe **(Figure 4.1 (c))** which are indexed by comparing the reflections with JCPDS card no. 89-4089 (γ-MnSe) and 40-1288 (β-MnSe).

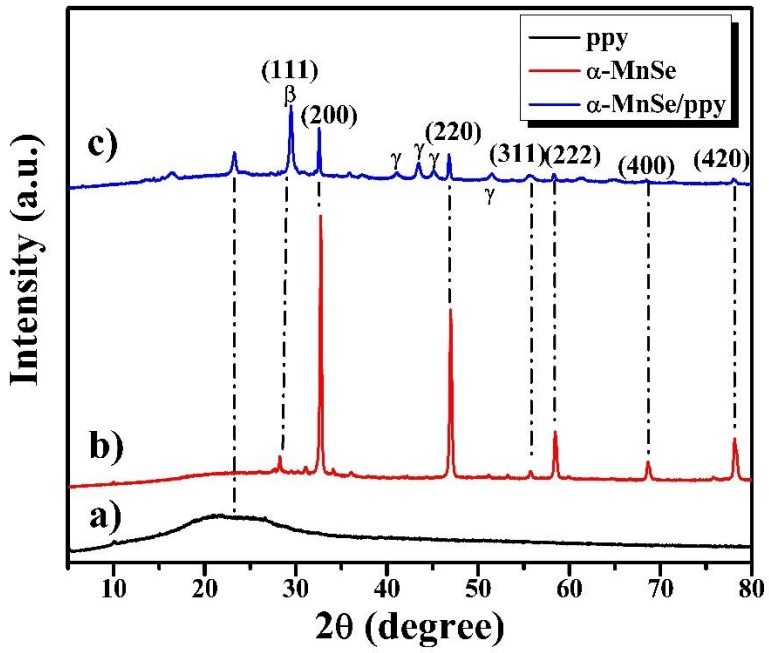

Figure 4.1. XRD patterns of **a)** ppy, **b)** α-MnSe, **c)** α-MnSe/ppy.

The overall intensity of XRD patterns decreases as ppy is dispersed over the α-MnSe surface and not intercalated. This is confirmed from the difference in the d spacing before and after the ppy incorporation **(Table 4.1)** which is quite lesser [39] but the intensity of the peak corresponding to (111) plane is increased due to the overlapping of (111) plane of β phase [40]. Also this increase in the intensity of (111) plane shows the growth of α-MnSe/ppy composite along (111) direction is enhanced which is consistent with that in the reported literature [41,42].

Table 4.1. d spacing calculated from XRD data.

Catalyst	2θ (degree)	d spacing (nm)
α-MnSe	29.01	0.31
	32.74	0.27
	47.00	0.19
	58.49	0.16
	78.22	0.12
α-MnSe/ppy	29.47	0.30
	32.56	0.28
	46.83	0.19
	58.33	0.15
	77.50	0.13

The ppy is responsible for the wide peaks at low angles, and α-MnSe crystalline peaks are also visible. The XRD patterns' existence of both crystalline and amorphous peaks attests to the α-MnSe/ppy composites' development.

4.5.1.2. FE-SEM

The surface morphology of the α-MnSe/ppy composite was examined through FE-SEM imaging across various magnifications, as depicted in **Figure 4.2 (a)** and **(b)**. Notably, a rod-like structure was observed, characterized by a rugged surface texture attributed to the presence of polypyrrole (ppy). Grain distribution in composite is notably diverse, and there is a visible agglomeration. Furthermore, the composite's grains are clearly separated from one another. The incorporation of polypyrrole introduces surface roughness to the α-MnSe material, a crucial aspect for enhancing OER activity [43]. This increase in roughness facilitates the creation of additional active sites and enlarges the surface area, both of which are pivotal for enhancing OER performance. Moreover, the EDS analysis **(Table 4.2)** and elemental mapping data, provided in **Figure 4.3** and **4.4** respectively, further support these findings.

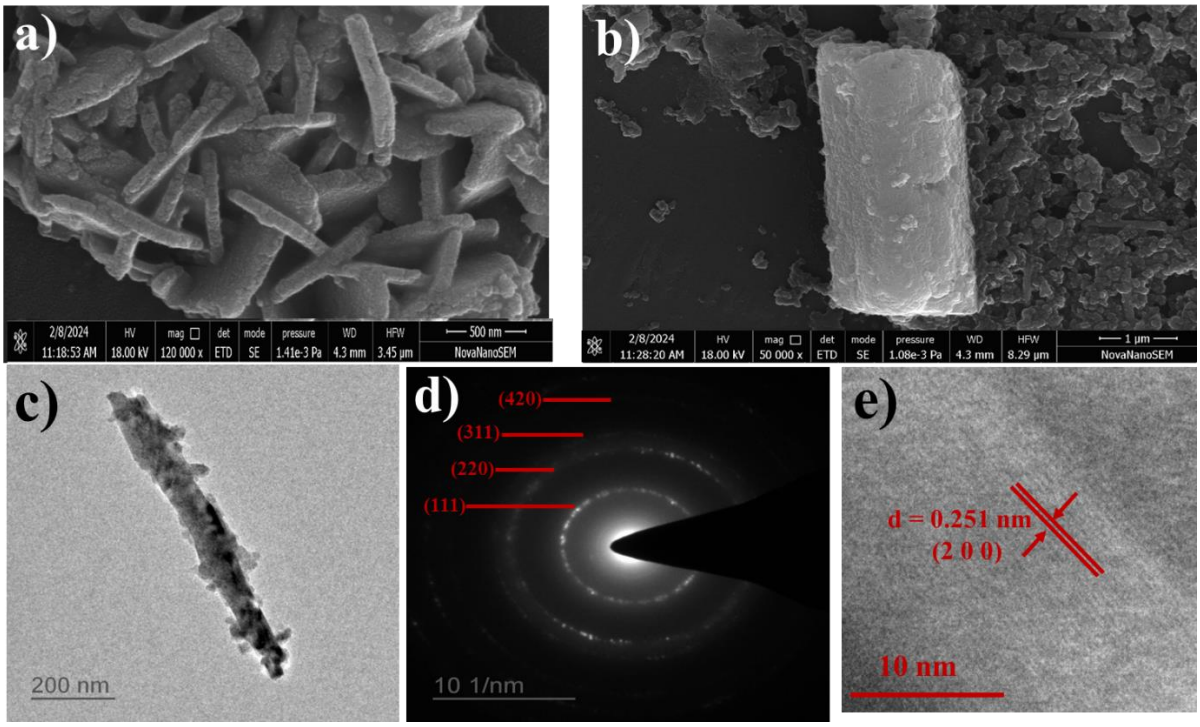

Figure 4.2. a, b) SEM images of α-MnSe/ppy, **c)** TEM image of α-MnSe/ppy, **d)** SAED pattern, **e)** HR-TEM image of α-MnSe/ppy.

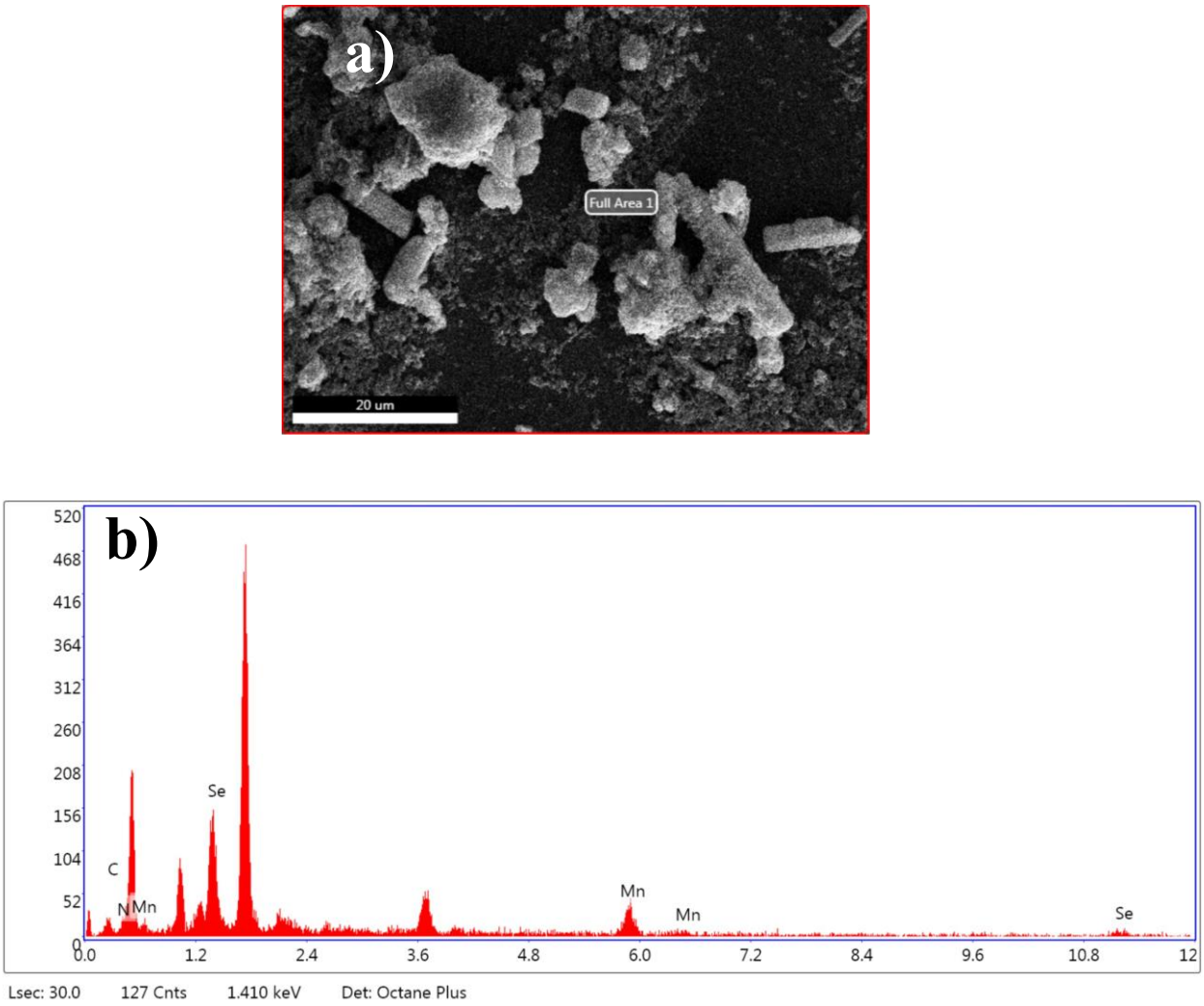

Figure 4.3. a) FE-SEM image of α-MnSe/ppy, **b)** Corresponding EDS spectra.

Table 4.2. Elemental composition from EDS spectra.

Element	Weight %	Atomic %	Net Int.	Error %	Kratio	Z	A	F
C K	15.20	33.68	6.38	15.10	0.0646	0.8157	0.5211	1.0000
N K	21.37	40.59	6.77	17.97	0.0756	0.7900	0.4481	1.0000
SeL	33.84	11.40	31.07	6.19	0.1961	0.5374	1.0782	0.9998
MnK	29.59	14.33	15.35	13.73	0.1975	0.6401	1.0114	1.0310

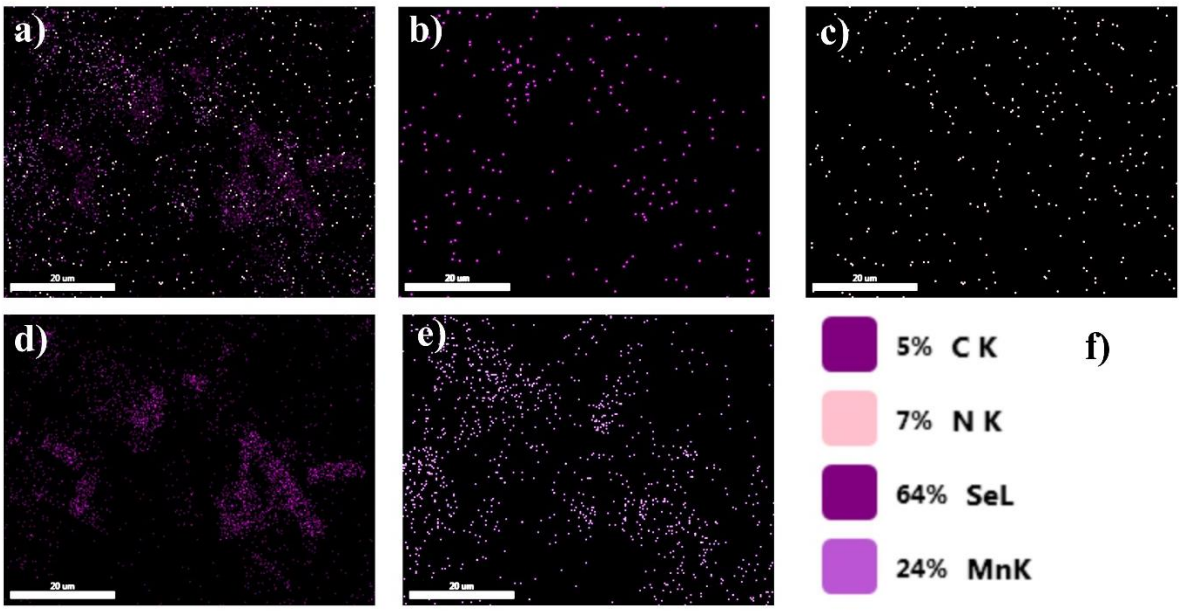

Figure 4.4. Elemental mapping.

4.5.1.3. HR-TEM

The TEM technique was used to study the intricate microstructure of the α-MnSe/ppy composite. **Figure 4.2 (c)** demonstrate that α-MnSe particle, with an average diameter of around 80–90 nm, are unevenly covered by ppy fibers, that improves the surface to provide more active sites and this also aligns with the results obtained from SEM analysis. The selected area electron diffraction (SAED) pattern **(Figure 4.2 (d))** obtained from the targeted region reveals the presence of dots and rings, which suggests that the α-MnSe/ppy composite have a polycrystalline as well as amorphous nature. The high-resolution transmission electron microscopy (HR-TEM) image **(Figure 4.2 (e))** of a single α-MnSe/ppy particle reveals distinct lattice fringes with interplanar spacing of 0.251 nm. This spacing correspond to the (2 0 0) crystal plane of the α-MnSe/ppy material.

4.5.2. Electrochemical characterizations

4.5.2.1. OER study

The OER performance of the prepared catalysts was extensively examined and compared utilizing LSV (Linear Sweep Voltammetry), CV (Cyclic Voltammetry), EIS (Electrochemical Impedance Spectroscopy), and Tafel slope analysis. **Figure 4.5 (a)** shows the LSV curves, recorded at 0.5 mV s^{-1} scan rate, for prepared catalysts, having least overpotential **(Figure 4.5 (c))** and highest current density for α-MnSe/ppy composite material than its individual counterparts and with the other catalysts previously reported in the literature **(Table 4.3)**. This must be happened because of the enhanced surface modification and roughness created by the heterostructure that increase the active sites for the OER intermediate species which is clear from the SEM images **(Figure 4.2 (a))**.

Table 4.3. Comparison of various parameters of electrocatalytic OER for Mn based materials reported in the literature.

Material	Synthesis technique	Support electrode	Overpotential (mV) / 10 mA cm^{-2}	Tafel slope / mV dec^{-1}	Electrolyte	References
$Mn_{0.1}Fe_{0.9}Se_2$	Hydrothermal	GPE	133	-	1 M KOH	[44]
$(CoMn)Se_2$	Anion exchange	RDE	270	39	1 M KOH	[45]
MnS_xSe_{1-x}@N,F-CQDs	Hydrothermal	GCE	209	72.18	1 M KOH	[46]
T(Ni_3S_2/MnS-O)	Hydrothermal	NF	228	41	1 M KOH	[47]
α-MnS	Hydrothermal	SS	292	70	1 M KOH	[48]
In_2MnSe_4	Ion Exchange	NF	259	86	1 M KOH	[49]
MnSe@MWCNT	Hydrothermal	RRDE	290	54.76	1 M KOH	[50]
MnFeSe	Hydrothermal	NF	247	35	1 M KOH	[51]
(MnCo)Se	Thermal	NF	243	62	1 M KOH	[52]

MnSe@MOF-5	Hydrothermal	NF	170	61	1 M KOH	[53]
$MnFeSe_2$	Hydrothermal	Ni Foil	190	59.2	1 M KOH	[54]
α-MnSe/ppy	Hydrothermal and solid state	FTO	168	67	1 M KOH	This work

To normalize the electrode roughness and material loading on the substrate, the activity was also calculated in terms of true current density and current density per mg (specific current density) [55]. Apparent current density (j_{app}), true current density (j_{true}), and specific current density (j_{spec}) values, together with the estimated values of overpotential (at denoted current densities) for prepared catalysts are listed in **Table 4.4**. Either apparent current density (j_{app}) or true current density (j_{true}), normalized by the geometric surface area of the electrode or the oxide roughness factor, could be used to represent the rate of electrochemical oxygen evolution. Overpotentials (η) for FTO/α-MnSe/ppy and FTO/α-MnSe was found to be ~168 mV and 285 mV **(Table 4.4)** respectively, calculated from the **Equation 1.19 (Chapter 1)** which is very close to the overpotential of state of art catalysts RuO_2 (240 mV) [56].

Additionally, in this study, the ECSA and R_f of these catalysts were calculated (From **Equation 1.22** and **1.24** from **Chapter 1**). The R_f value offers insight into the topology and distribution of active sites. R_f greater than 1 indicates a larger and more favorable absorption area [57]. This research shows that catalysts with R_f values above one has favorable adsorption surface areas. ECSA was determined using suitable formulae **(Equation 1.22)**, with α-MnSe/ppy demonstrating a larger C_{dl} value (183.45 μF cm^{-2}) and ECSA (2.29 cm^2) compared

to its counterparts **(Figure 4.6 (d))** suggesting a more electrochemically active surface area, where C_{dl} is a double layer capacitance. Elevated ECSA values demonstrated that the composite included increased exposed active sites, which partake in electrolysis and were essential for electron–proton transport between the electrolyte and the electrode [58]. For calculating the double layer capacitance, CV in non-faradaic region (1.15 V – 1.20 V vs. RHE) at varying scan rates ranging from 20 mV s^{-1} to 100 mV s^{-1} **(Figure 4.5 (b))** was conducted and plot of scan rate vs. current density is plotted to obtain a straight line **(Figure 4.5 (e))** and half of the slope of the straight line gives the measure of C_{dl} **(Equation 1.23)** [59].

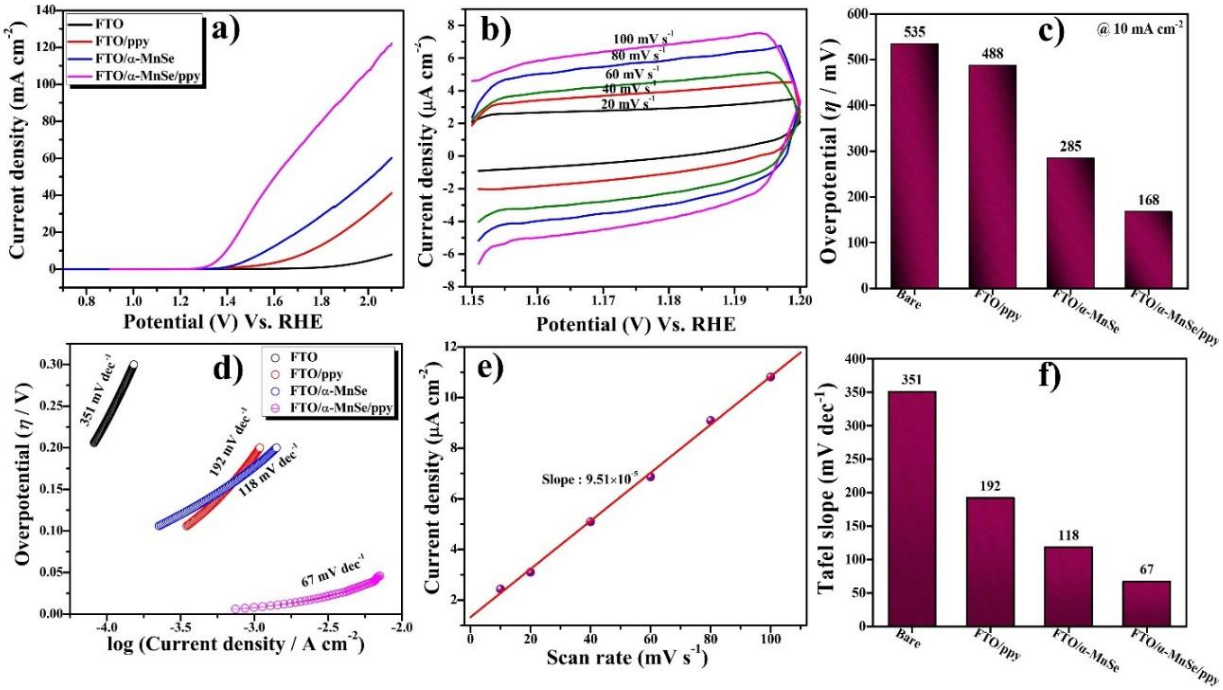

Figure 4.5. a) LSV at 0.5 mV s^{-1} scan rate in 1 M KOH at 25 ºC, **b)** CV of FTO/α-MnSe/ppy electrode in non-faradaic region at different scan rates, **c)** Variation of overpotential with as prepared catalysts and bare electrode, **d)** Tafel slopes, **e)** Corresponding C_{dl} plot for FTO/α-MnSe/ppy electrode **f)** Variation of Tafel slopes with as prepared catalysts and bare electrode.

Table 4.4. Electrode kinetic parameters

Electrode	Overpotential (mV) at 10 mA cm^{-2}	Current density at E = 2.0 V vs. RHE (mA cm^{-2})			C_{dl} (μF cm^{-2})	R_f	ECSA (cm^2)	Tafel Slope (mV dec^{-1})
		j_{app}	j_{true}	$j_{specific}$				
Bare	535 (η_1)	4.87	4.68	14.75	41.60	1.04	0.52	351
FTO/ppy	488	31.31	35.91	94.88	34.88	0.87	0.44	192
FTO/α-MnSe	285	51.30	11.18	155.45	47.56	1.19	0.60	118
FTO/α-MnSe/ppy	168	106.90	89.91	323.94	183.45	4.59	2.29	67

The Tafel slope, which is a measure of catalytic activity, was calculated using the analytical Tafel equation ($\eta = b \log j$) [60]. α-MnSe/ppy had the most favorable catalytic activity among its other counterparts, as seen by its much lower Tafel slope value of 67 mV dec^{-1} **(Figure 4.5 (d))**. For efficient electrocatalysts, a low Tafel slope value is desired. α-MnSe/ppy displayed the lowest Tafel slope of 67 mV dec^{-1} among other prepared catalysts proving the faster kinetics for the same among the other counterparts **(Figure 4.5 (f))**. Tafel slopes of other counterparts and bare electrode are given in the **Table 4.4** for comparison. This proximity to the highlighted Tafel slope of 60 mV dec^{-1} implies that the rate-determining phase

may entail H_2O removal and O* creation (**Equation (4.2)** of the OER mechanism) [61]. The larger current density and lower Tafel slope of α-MnSe/ppy were further corroborated by the Nyquist plots, confirming its lowest R_{ct}, thus compared to other variations.

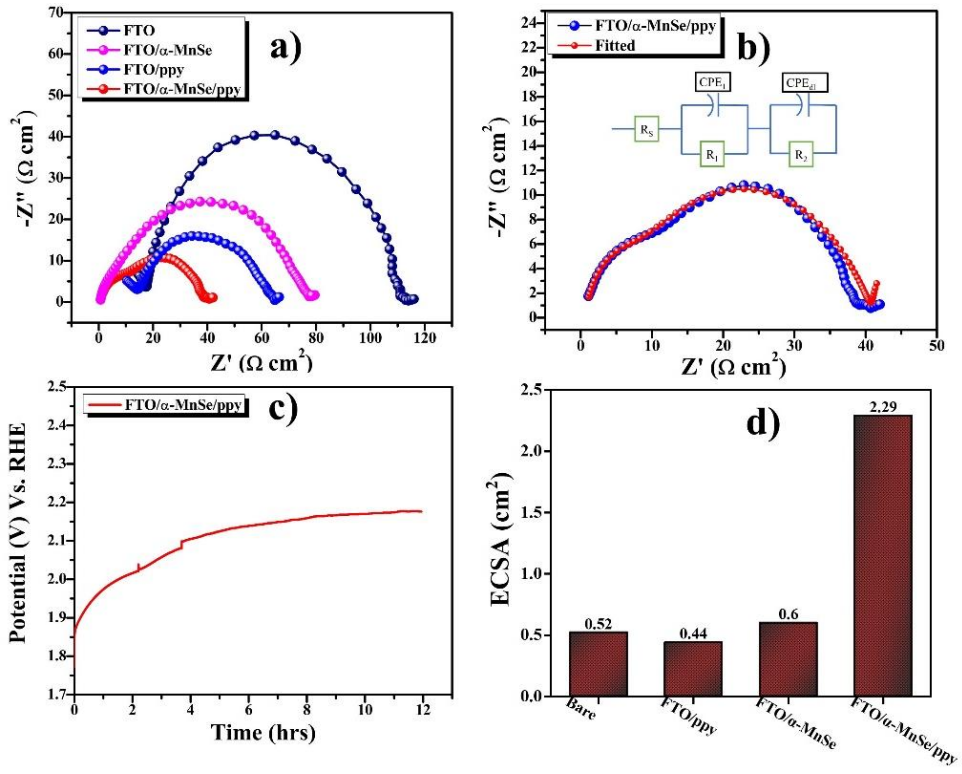

Figure 4.6. a) Nyquist plots, **b)** Fitted Nyquist plot of FTO/α-MnSe/ppy electrode, **c)** Chronopotentiometry response for FTO/α-MnSe/ppy electrode, **d)** Variation of ECSA with as prepared catalysts and bare electrode.

In addition, the rate at which charge is transferred between the adsorbed intermediates at the electrode interface was evaluated using electrochemical impedance spectroscopy (EIS), which is shown graphically as Nyquist plots **(Figure 4.6 (a))**. Typically, the development of a semicircle on the Z_{real} -axis implies resistance to charge transfer (R_{ct}), that includes solution

resistance if the curvature comes from the origin [62]. Comparing α-MnSe/ppy with α-MnSe, and ppy, it demonstrated the shortest semicircle curvature, indicating the least barrier to charge transfer during OER.

The semicircles in Nyquist plots at various frequency regions reflects the adsorption/desorption of reactive intermediates (H^+/OH^-) and charge transfer resistance (R_{ct}) [63,64]. The semicircles appear in order of increasing time constant and decreasing relaxation frequency. Parallel RC circuits with smaller RC time constants (smaller products) will appear first at higher frequencies, while processes with larger time constants will appear later at lower frequencies [65]. In **Figure 4.6 (b)**, the first semicircle in the EIS spectrum originates from the impedance of the film resistance, which forms at the interface between the electrode and electrolyte due to electrolyte decomposition and this resistance is independent of potential change which is confirmed by the inset **Figure 4.7 (b)** [66].

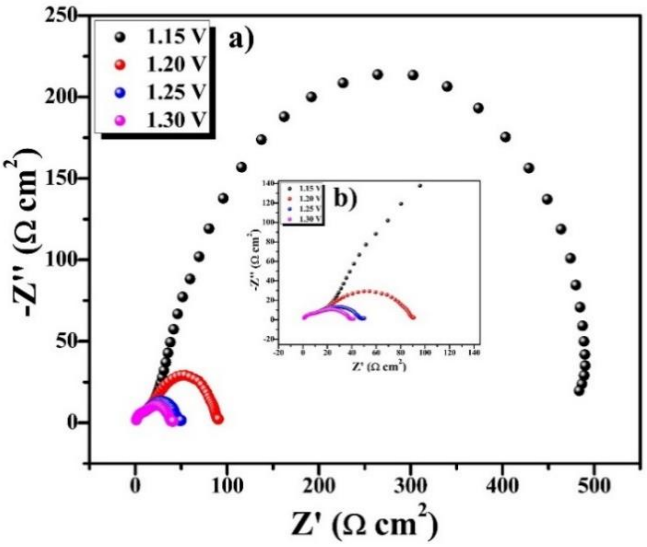

Figure 4.7. a) Nyquist plots of FTO/α-MnSe/ppy electrode on increasing potential, **b)** magnified image of the Nyquist plots at high frequencies.

The second semicircle in the EIS results is associated with the charge transfer resistance (R_{ct}), which is related to the kinetics of an electrochemical reaction and is affected by factors such as surface coating, phase transition, bandgap structure, and particle size [67–70]. The diameter of this semi-circle decreases as we increase potential which is shown in **Figure 4.7 (a)**. Since the rate of charge transfer increases on increasing potential, the resistance must decrease which is confirmed by the **Figure 4.7 (a)**.

These EIS results are compatible with LSV experiments and give thorough insights into the catalytic performance of the materials. The Nyquist plot is evaluated based on an analogous circuit model, as illustrated in the inset in **Figure 4.6 (b)**. This model comprises R_s, representing solution resistance, R_1, showing electrode surface resistance from the catalyst to the electrode at the interface; and R_{ct}, expressing charge transfer resistance [71,72]. Honglin Ai *et al.* reported the similar circuit fitting for Co_3O_4/ppy composite, showing one depressed semi-circle in high frequency region that corresponds to film resistance and second semi-circle related to charge transfer resistance [73]. Similarly, Jing He *et al.* investigated a triple-layered PPy@NiCo-LDH/$FeCo_2O_4$ for OER and found similar circuit fitting for EIS data [74]. Generally, a lower R_{ct} value suggests a faster electron transfer process.

Analysis of the fitting data indicates that α-MnSe/ppy displays the lowest R_{ct} value of 20.9 Ω. In contrast, α-MnSe and ppy have R_{ct} values of 30.55 Ω and 50.70 Ω, respectively. This shows that α-MnSe/ppy displays optimum charge transfer efficiency and increased catalytic activity. Such synergistic effects lead to lower charge transfer resistance at the electrolyte-electrode interface, hence boosting overall charge transport performance and decreasing interfacial resistance. The other circuit parameters are given in the **Table 4.5**.

Table 4.5. Circuit parameters

Electrode	Solution resistance (R_s) (Ω)	Electrode surface resistance (R_1) (Ω)	Charge transfer resistance (R_2) (Ω)
Bare	4.99	13.35	99.14
FTO/ppy	7.81	8.65	50.70
FTO/α-MnSe	1.11	11.35	30.55
FTO/α-MnSe/ppy	0.77	6.90	20.90

4.5.2.2. Thermodynamic study

Electrodes made of FTO/α-MnSe/ppy and their counterparts along with bare FTO were investigated in order to determine the standard electrochemical energy of activation ($\Delta H_{el}^{0\neq}$), standard entropy of activation ($\Delta S^{0\neq}$), and standard enthalpy of activation ($\Delta H^{0\neq}$). This required keeping the reference electrode at a constant 25 ºC throughout the experiment while recording anodic polarization curves in 1 M KOH at temperatures ranging from 25 ºC to 55 ºC **(Figure 4.8 (a))** and corresponding Arrhenius plots were obtained **(Figure 4.8 (b))**. α-MnSe and ppy comparative data are shown in **Table 4.6**. As expected, it can be seen that FTO/α-MnSe/ppy electrode had a lower electrochemical activation energy among others. This indicates the

composite material needs lesser energy to proceed the reaction than the others. According to the relation $\alpha = 2.303RT/bF$, where R is the gas constant, F is the Faraday constant, and T is the absolute temperature, the average value of the transfer coefficient α of α-MnSe/ppy was close to unity. Additional thermodynamic parameters were determined using relevant relations **(Equation 1.27 and 1.29** from **Chapter 1)**, and **Table 4.6** lists their average values. The Tafel slope (b) was obtained from the polarization curve acquired at different temperatures and expressed in mV dec^{-1}. Planck's constant (h) and the Boltzmann constant (k_B) were added to the frequency term to get k_BT/h.

The commencement of adsorption for the electrochemical generation of oxygen is highest for FTO/α-MnSe/ppy electrode indicating the more active sites for the adsorption of reactive species, in accordance with the most negative value of $\Delta S^{0\neq}$.

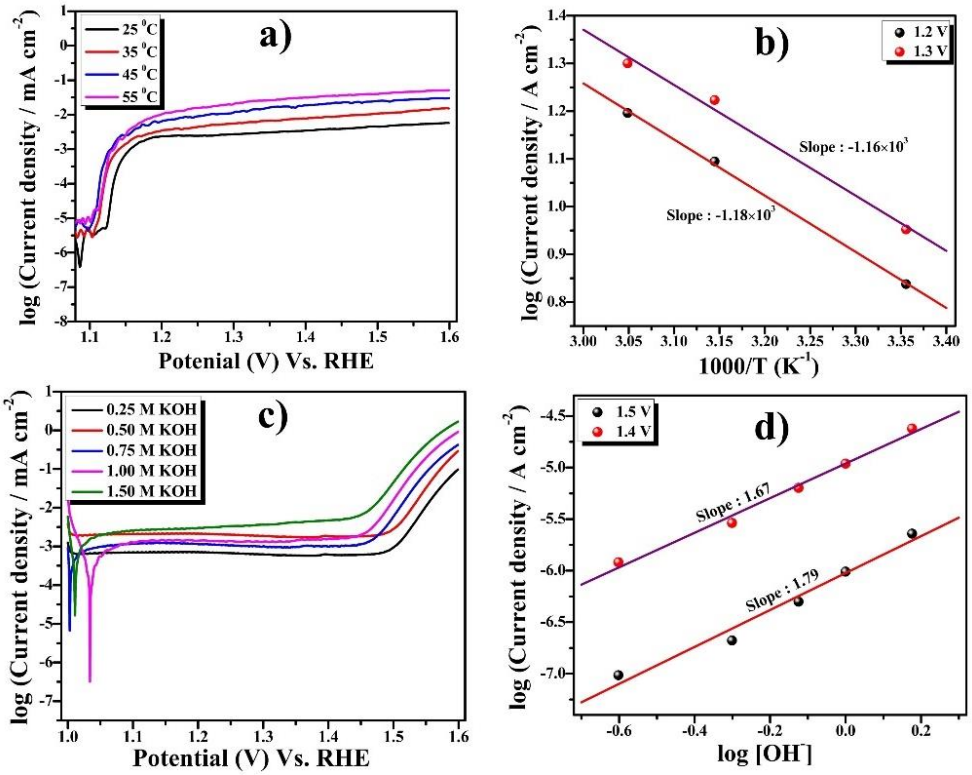

Figure 4.8. a) Tafel polarization curves of FTO/α-MnSe/ppy electrode at different temperatures, **b)** Corresponding Arrhenius plot, **c)** Tafel polarization curves of FTO/α-MnSe/ppy electrode at different concentrations of KOH **d)** order of reaction.

All the plots and measurements made for all the other prepared catalysts (α-MnSe and ppy) and bare FTO electrode are given below in **Figures 4.9** (α-MnSe)**, 4.10** (ppy), **and 4.11** (bare FTO).

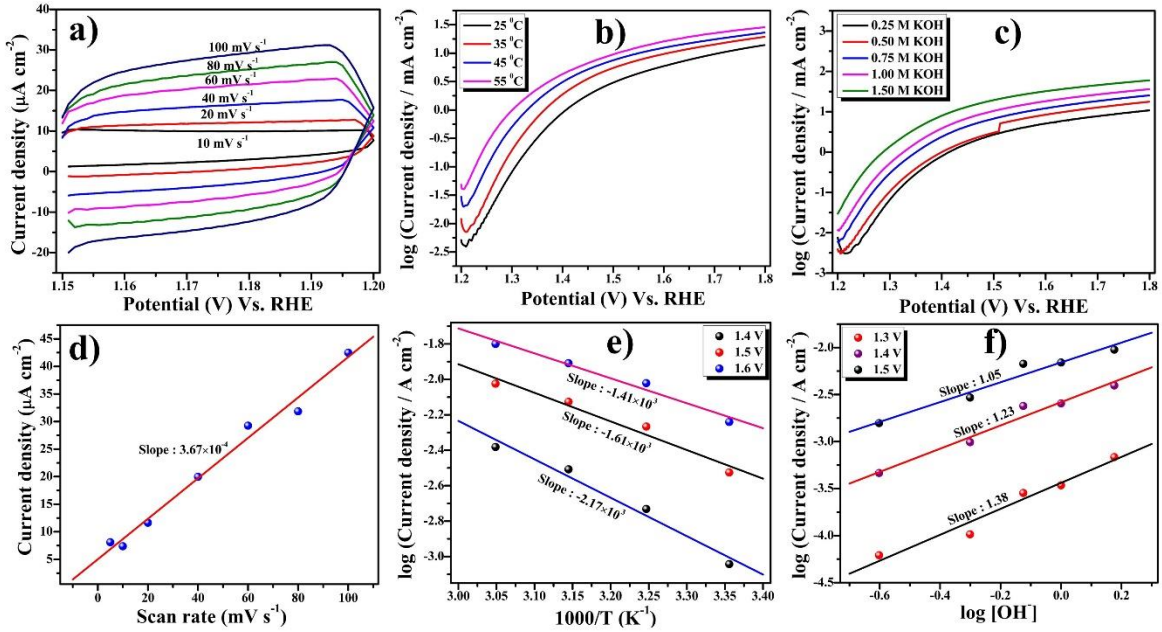

Figure 4.9. a) CV of FTO/α-MnSe electrode in non-faradaic region at different scan rates, **b)** Tafel polarization curves of FTO/α-MnSe electrode at different temperatures, **c)** Tafel polarization curves of FTO/α-MnSe electrode at different concentrations of KOH, **d)** Corresponding C_{dl} plot for FTO/α-MnSe electrode, **e)** Corresponding Arrhenius plot for FTO/α-MnSe electrode, **f)** order of reaction for FTO/α-MnSe electrode.

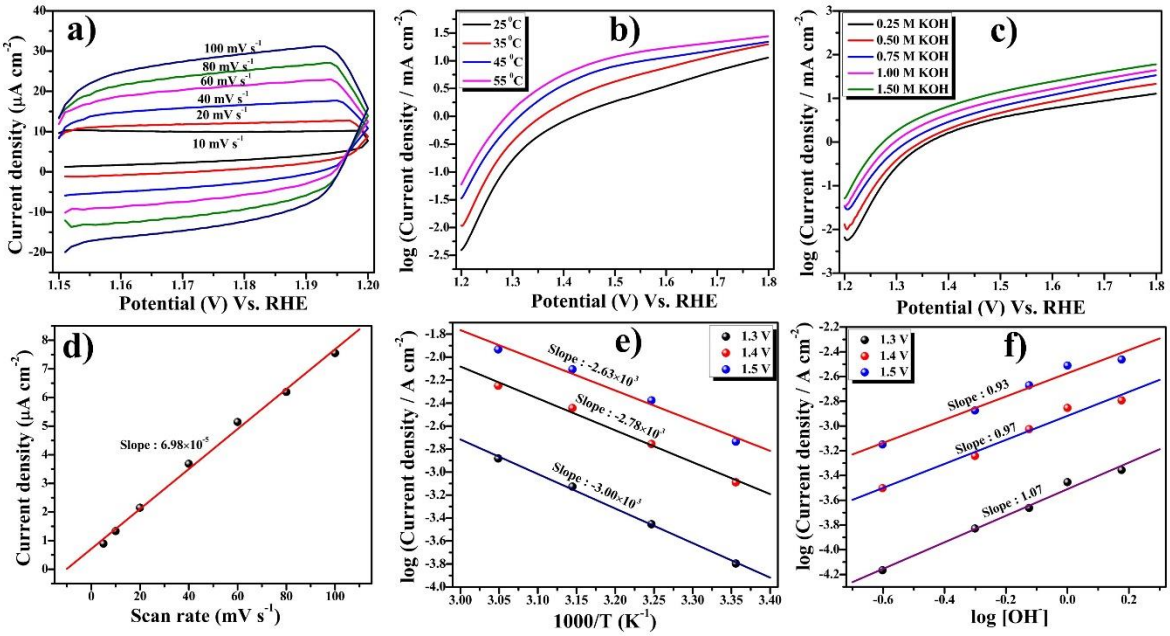

Figure 4.10. a) CV of FTO/ppy electrode in non-faradaic region at different scan rates, **b)** Tafel polarization curves of FTO/ppy electrode at different temperatures, **c)** Tafel polarization curves of FTO/ppy electrode at different concentrations of KOH, **d)** Corresponding C_{dl} plot for FTO/ppy electrode, **e)** Corresponding Arrhenius plot for FTO/ppy electrode, **f)** order of reaction for FTO/ppy electrode.

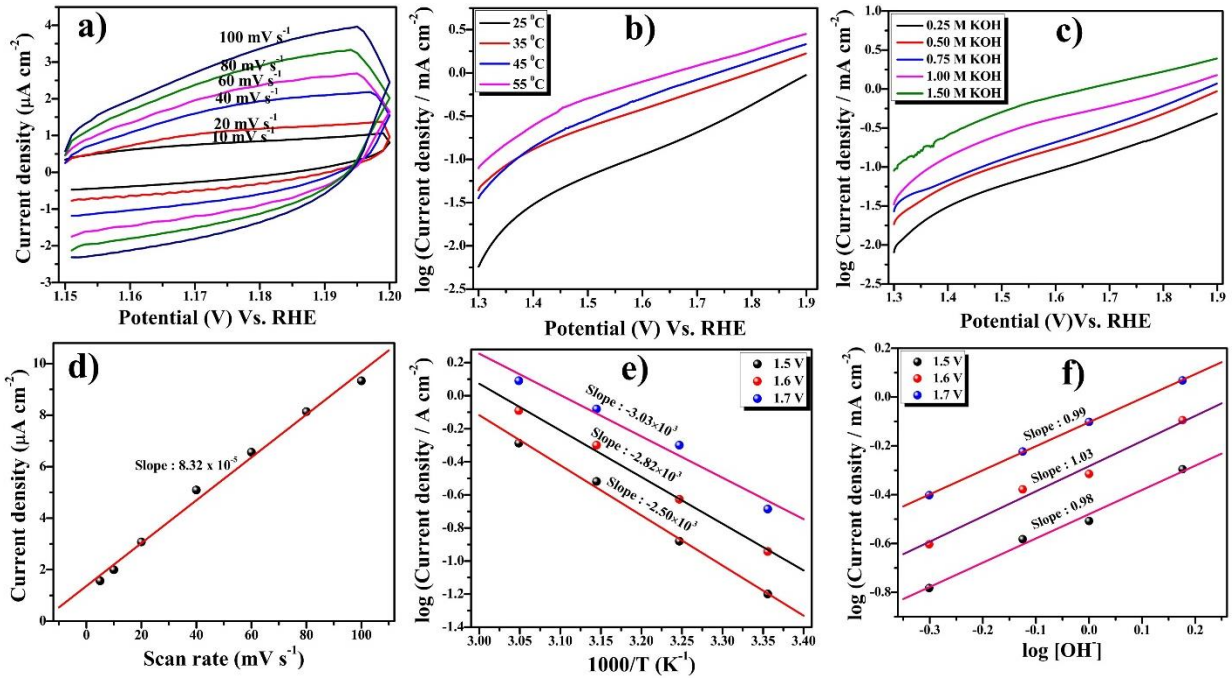

Figure 4.11. a) CV of bare FTO electrode in non-faradaic region at different scan rates, **b)** Tafel polarization curves of bare FTO electrode at different temperatures, **c)** Tafel polarization curves of bare FTO electrode at different concentrations of KOH, **d)** Corresponding C_{dl} plot for bare FTO electrode, **e)** Corresponding Arrhenius plot for bare FTO electrode, **f)** order of reaction for bare FTO electrode.

Table 4.6. Thermodynamic parameters

Electrode	Standard electrochemical energy of activation ($\Delta H_{el}^{0\neq}$) (kJ mol^{-1})	Standard electrochemical entropy of activation ($-\Delta S_{el}^{0\neq}$) (J K^{-1}mol^{-1})	Transfer coefficient (α)	Standard enthalpy of activation ($\Delta H^{0\neq}$) (kJ mol^{-1})
Bare	47.90	67.97	0.17	80.71
FTO/ppy	50.28	42.31	0.31	110.11
FTO/α-MnSe	26.94	116.80	0.50	123.44
FTO/α-MnSe/ppy	22.17	122.35	0.88	169.84

4.5.2.3. OER mechanism

Using the methods described in the literature [75], the OER order by changing OH^- concentration was ascertained. For each catalyst, the values were found non integral which in not unusual and are already reported by several works [76,77]. This has been explained by considering the OH^- adsorption/ionization of surface hydroxyl groups [78] and the total surface

coverage by adsorbed intermediates (i.e. oxygen containing species) formed during the electro formation of oxygen under Temkin adsorption condition [79,80]. Tafel polarization curves were recorded on individual prepared electrodes in order to determine the order **(Figure 4.8 (c))**. In this study, varying KOH concentrations from 0.25 M to 1.25 M were used by maintaining the ionic strength constant using neutral electrolyte KNO_3.

From these curves, linear log (current density) vs. log [OH^-] curves were made by examining polarization curves acquired at various KOH concentrations at different potentials **(Figure 4.8 (d))**. The slope of these straight lines was then measured to establish the order of reactions.

Four electrochemical steps, including one proton transfer in an alkaline media, are often involved in the OER process. The process starts at the metal's (M) active sites with the adsorption and release of OH^-, then moves on to the electro-sorption of OH^- ions **(Equation (4.1))**. Then, an O-O bond is formed as a result of a sequence of intermediates, including OH*, O*, OOH*, and OO*, being adsorbed on the metal's (M) active sites, which are marked by M-O bonding **(Equations (4.2), (4.3), (4.4))**. According to earlier research, these chemical stages are connected to the OER process [60,81].

$$OH^- + M \rightarrow M + OH^* + e^- \qquad \textbf{(4.1)}$$

$$OH^* + OH^- \rightarrow O^* + H_2O + e^- \qquad \textbf{(4.2)}$$

$$OH^- + O^* \rightarrow OOH^* + e^- \qquad \textbf{(4.3)}$$

$$OH^- + OOH^* \rightarrow O_2 + H_2O + e^- \qquad \textbf{(4.4)}$$

This mechanism is similar to the electrochemical path proposed by Bockris [79], which is based on AEM (already discussed in **Chapter 1**). Nonetheless, it is important to recognize

the plausible presence of substitute pathways, such as Bockris-Otagawa's peroxide route, and Krasil'shchikov's pathway [79]. According to the suggested process, O* and OH* function as surface-adsorbed intermediates, while 'M' (=Mn) serves as an active site on the surface.

It is noteworthy to mention that the selenide serves as "pre-catalyst" for the OER in high pH environments. It has been discovered that at the facade of the catalyst, portion of Mn from α-MnSe converts to MnOOH, acting as the actual-time OER catalyst [82].

4.5.2.4. Stability and durability

To ensure practical suitability and commercialization, a catalyst must not only exhibit superior catalytic activity but also demonstrate enhanced stability over prolonged use. Thus, assessing the long-term stability and durability of an electrocatalyst is crucial. The stability of FTO/α-MnSe/ppy electrode was evaluated through chronopotentiometry tests in a 1 M KOH electrolyte. The chronopotentiometry shows an increment in overpotential till few hours because the newly formed oxygen bubbles create resistance at the surface of the electrode and to overcome this resistance it needs some extra potential to achieve equilibrium [83,84]. Once equilibrium is reached, FTO/α-MnSe/ppy electrode displayed consistent stability, with less significant change in potential over the period of 12 hrs as shown in **Figure 4.6 (c)**. This consistency suggests that the FTO/α-MnSe/ppy electrode retains its catalytic activity even amidst gas bubble evolution.

4.5.3. *Operando* Spectro-electrochemical study

UV-Vis spectroscopy is a widely employed technique for investigating the optical properties and reaction kinetics of catalysts, especially those that are homogeneous or molecularly

heterogeneous [85]. When integrated with electrochemical experiments, this method is termed UV-Vis spectro-electrochemistry (SEC) [86–89]. In UV-Vis SEC, the oxidation states and concentration changes of catalysts can be monitored by measuring their unique absorption spectra, and these can be quantified using the well-known Lambert-Beer's law as already discussed in **Chapter 2** (**Equation (2.1))**.

In UV-Vis SEC, absorbance is recorded while simultaneously monitoring the current through the circuit. This allows for correlating the current and optical responses with respect to the applied potential and varying electrolyte environments and reaction conditions. Although UV-Vis SEC has been predominantly utilized for studying molecular systems, it is also applicable to electrodes [90–92]. To examine specific redox reactions (oxidation or reduction), the method is typically conducted in a three-electrode cell configuration [93].

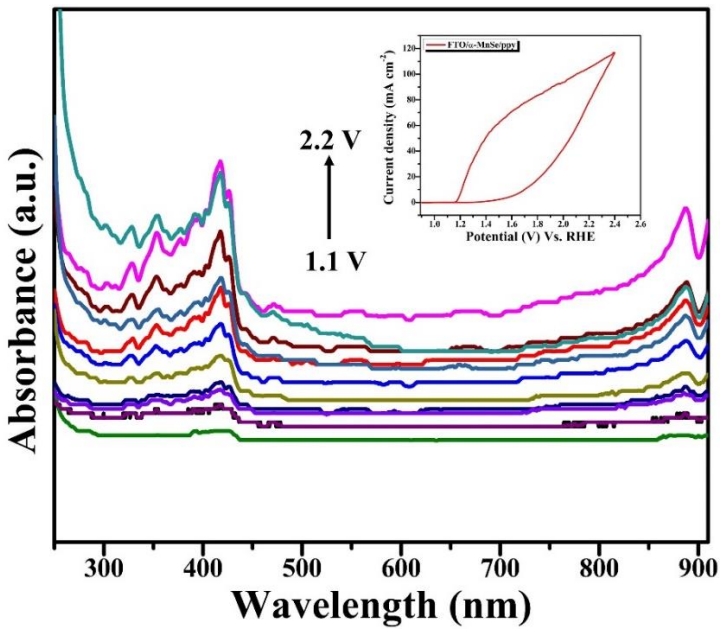

Figure 4.12. *Operando* UV-vis spectra of FTO/α-MnSe/ppy during cyclic voltammetry at scan rate of 20 mV s^{-1}.

UV-vis–NIR spectroscopy experiments conducted under conditions relevant to the OER have revealed an intriguing observation: as the voltage increases to the onset potential in the OER region, there is a corresponding increase in absorbance. This phenomenon was first explored by Conway in the late 1950s. He discovered that oxygen evolution occurred simultaneously with the reduction of oxidized species as the potential dropped from OER-relevant levels to open-circuit potentials. This finding suggests that these oxidized states can be reduced to generate molecular oxygen [94]. Oxo species located on adjacent metal centers might chemically interact to produce molecular oxygen. This process is akin to the OER observed for cobalt in a phosphate electrolyte [95–97] and CoOOH [98,99]. *Operando* UV-vis spectroscopy measurements were performed to explore the reactive intermediates during OER and elucidate the observed activity patterns. [100]. **Figure 4.12** depicts the *operando* UV-Vis spectroscopy before and during the cyclic voltammetry for the FTO/α-MnSe/ppy electrode performed at 25 ºC in 1 M KOH at scan rate of 20 mV s^{-1}, respectively. Upon stepping the electrode potential from 1.2 V to 2.2 V vs. RHE in 0.1 V increments, the formation of absorption peaks from 300-440 nm and a small peak from 850-900 nm were observed, and these absorbance peaks broadened and intensified with increase of applied potential. These may correspond to MnOOH species [101] when O_2 evolution is proceeding on the electrode.

The changes in the UV to visible spectral range include excitation transitions of various oxidation states of Mn atoms as follows: $^6A_{1g} \rightarrow {}^4T_{1g}$, of Mn^{2+} at approximately 340 nm [102,103], $^5E_{1g} \rightarrow {}^5T_{2g}$ of Mn^{3+} at 500 nm [104], $^4A_2 \rightarrow {}^4T_{2g}$ of Mn^{4+} at 460 nm, and $^3A_2 \rightarrow {}^3T_2$ of Mn^{5+} at 720 nm [105,106]. In the NIR spectral range, there are combined stretching and deformation vibrations of hydrogen-bonded water molecules to surface OH groups at 850 to

900 nm [107,108]. The formation of various intermediates in the OER is reflected in the process. Oxygen evolution is known to occur through a series of one-electron intermediates, beginning with the formation of $–OH^–$ and leading to the sequential formation of $=O^{2–}$, $–OOH^–$, and $–OO^{2–}$. It should be noted that the NIR signals do not directly provide the spectroscopic signatures of these intermediates. Instead, their formation is inferred from the potential-dependent changes in the vibrational intensity of Mn–OH [109].

4.6. Conclusion

The catalysts were assessed for their potential as electrocatalysts in promoting the OER in an alkaline medium (1 M KOH). Experimental results demonstrated that α-MnSe/ppy can be synthesized cost-effectively and straightforwardly using a hydrothermal process followed by solid-state grinding. Notably, the Tafel slope was found to be the lowest for FTO/α-MnSe/ppy electrode, indicating its superior electrocatalytic activity for OER in an alkaline environment. This catalyst exhibited nearly second-order kinetics for the OER process. Among the tested catalysts, α-MnSe/ppy had the lowest standard electrochemical activation energy, reinforcing its efficacy. *Operando* spectro-electrochemical analysis identified the active sites for OER, as evidenced by the formation of absorption peaks between 300-440 nm, which are attributed to MnOOH species. Further investigation in the NIR region is required to fully understand the role of these redox-active sites. The study revealed that multiple redox species form during the OER, which contribute to the electrocatalytic performance of α-MnSe/ppy, with this material showing the highest absorbance intensity. *Operando* UV-Vis spectroscopy remains an underutilized technique for the identification and characterization of reactive intermediate species in catalytic processes. Despite its potential to provide real-time insights into reaction

mechanisms under actual operating conditions, only a limited number of studies have employed this method. Therefore, further comprehensive investigations are essential to fully explore its capabilities and establish it as a powerful tool for advancing our understanding of catalytic pathways in future research.

Additionally, α-MnSe/ppy and similar materials show promise as electrode materials for energy storage devices and other applications. By utilizing efficient OER catalysts, large-scale practical water splitting can be achieved, providing the clean and efficient energy needed to meet modern demands.

4.7. References

[1] I. Ganesh, Conversion of carbon dioxide into methanol - A potential liquid fuel: Fundamental challenges and opportunities (a review), Renew. Sustain. Energy Rev. 31 (2014) 221–257. https://doi.org/10.1016/j.rser.2013.11.045.

[2] J. Blanco, S. Malato, P. Fernández-Ibañez, D. Alarcón, W. Gernjak, M.I. Maldonado, Review of feasible solar energy applications to water processes, Renew. Sustain. Energy Rev. 13 (2009) 1437–1445. https://doi.org/10.1016/j.rser.2008.08.016.

[3] M. Pudukudy, Z. Yaakob, M. Mohammad, B. Narayanan, K. Sopian, Renewable hydrogen economy in Asia - Opportunities and challenges: An overview, Renew. Sustain. Energy Rev. 30 (2014) 743–757. https://doi.org/10.1016/j.rser.2013.11.015.

[4] I.R. Hamdani, A.N. Bhaskarwar, Recent progress in material selection and device designs for photoelectrochemical water-splitting, Renew. Sustain. Energy Rev. 138 (2021). https://doi.org/10.1016/j.rser.2020.110503.

[5] F. Abdelghafar, X. Xu, S.P. Jiang, Z. Shao, Designing single-atom catalysts toward improved alkaline hydrogen evolution reaction, Mater. Reports Energy. 2 (2022). https://doi.org/10.1016/j.matre.2022.100144.

[6] Y. Ma, X. Wang, Y. Jia, X. Chen, H. Han, C. Li, Titanium dioxide-based nanomaterials for photocatalytic fuel generations, Chem. Rev. 114 (2014) 9987–10043. https://doi.org/10.1021/cr500008u.

[7] C.R. Lhermitte, K. Sivula, Alternative Oxidation Reactions for Solar-Driven Fuel Production, ACS Catal. 9 (2019) 2007–2017. https://doi.org/10.1021/acscatal.8b04565.

[8] W. Zhang, W. Lai, R. Cao, Energy-Related Small Molecule Activation Reactions: Oxygen Reduction and Hydrogen and Oxygen Evolution Reactions Catalyzed by Porphyrin- and Corrole-Based Systems, Chem. Rev. 117 (2017) 3717–3797. https://doi.org/10.1021/acs.chemrev.6b00299.

[9] S. Zhao, Y. Wang, J. Dong, C.T. He, H. Yin, P. An, K. Zhao, X. Zhang, C. Gao, L. Zhang, J. Lv, J. Wang, J. Zhang, A.M. Khattak, N.A. Khan, Z. Wei, J. Zhang, S. Liu, H. Zhao, Z. Tang, Ultrathin metal-organic framework nanosheets for electrocatalytic oxygen evolution, Nat. Energy. 1 (2016). https://doi.org/10.1038/nenergy.2016.184.

[10] S. Li, Y. Gao, N. Li, L. Ge, X. Bu, P. Feng, Transition metal-based bimetallic MOFs and MOF-derived catalysts for electrochemical oxygen evolution reaction, Energy Environ. Sci. 14 (2021) 1897–1927. https://doi.org/10.1039/d0ee03697h.

[11] Y. Yu, J. Zhou, Z. Sun, Novel 2D Transition-Metal Carbides: Ultrahigh Performance Electrocatalysts for Overall Water Splitting and Oxygen Reduction, Adv. Funct. Mater. 30 (2020). https://doi.org/10.1002/adfm.202000570.

[12] S. Zhao, D.W. Wang, R. Amal, L. Dai, Carbon-Based Metal-Free Catalysts for Key Reactions Involved in Energy Conversion and Storage, Adv. Mater. 31 (2019). https://doi.org/10.1002/adma.201801526.

[13] S. Chandrasekaran, D. Ma, Y. Ge, L. Deng, C. Bowen, J. Roscow, Y. Zhang, Z. Lin, R.D.K. Misra, J. Li, P. Zhang, H. Zhang, Electronic structure engineering on two-dimensional (2D) electrocatalytic materials for oxygen reduction, oxygen evolution, and hydrogen evolution reactions, Nano Energy. 77 (2020). https://doi.org/10.1016/j.nanoen.2020.105080.

[14] X. Cao, T. Wang, L. Jiao, Transition-Metal (Fe, Co, and Ni)-Based Nanofiber Electrocatalysts for Water Splitting, Adv. Fiber Mater. 3 (2021) 210–228. https://doi.org/10.1007/s42765-021-00065-z.

[15] L. Wei, E.H. Ang, Y. Yang, Y. Qin, Y. Zhang, M. Ye, Q. Liu, C.C. Li, Recent advances of transition metal based bifunctional electrocatalysts for rechargeable zinc-air batteries, J. Power Sources. 477 (2020). https://doi.org/10.1016/j.jpowsour.2020.228696.

[16] T. Zhao, Y. Wang, S. Karuturi, K. Catchpole, Q. Zhang, C. Zhao, Design and operando/in situ characterization of precious-metal-free electrocatalysts for alkaline water splitting, Carbon Energy. 2 (2020) 582–613. https://doi.org/10.1002/cey2.79.

[17] H. Zhong, C.A. Campos-Roldán, Y. Zhao, S. Zhang, Y. Feng, N. Alonso-Vante, Recent advances of cobalt-based electrocatalysts for oxygen electrode reactions and hydrogen evolution reaction, Catalysts. 8 (2018). https://doi.org/10.3390/catal8110559.

[18] A. Garg, S. Basu, N.P. Shetti, K.R. Reddy, 2D materials and its heterostructured photocatalysts: Synthesis, properties, functionalization and applications in environmental remediation, J. Environ. Chem. Eng. 9 (2021). https://doi.org/10.1016/j.jece.2021.106408.

[19] C.Z. Yuan, K.S. Hui, H. Yin, S. Zhu, J. Zhang, X.L. Wu, X. Hong, W. Zhou, X. Fan, F. Bin, F. Chen, K.N. Hui, Regulating Intrinsic Electronic Structures of Transition-Metal-Based Catalysts and the Potential Applications for Electrocatalytic Water Splitting, ACS Mater. Lett. 3 (2021) 752–780. https://doi.org/10.1021/acsmaterialslett.0c00549.

[20] N.F.H. Nik Zaiman, N. Shaari, N.A.M. Harun, Developing metal-organic framework-based composite for innovative fuel cell application: An overview, Int. J. Energy Res. 46 (2022) 471–504. https://doi.org/10.1002/er.7198.

[21] X. Rui, H. Tan, Q. Yan, Nanostructured metal sulfides for energy storage, Nanoscale. 6 (2014) 9889–9924. https://doi.org/10.1039/c4nr03057e.

[22] H. Sato, T. Mihara, A. Furuta, Y. Ueda, H. Namatame, M. Taniguchi, Electronic structure of MnY (Y=S, Se, Te), J. Electron Spectros. Relat. Phenomena. 78 (1996) 87–90. https://doi.org/10.1016/s0368-2048(96)80033-8.

[23] I.T. Sines, R. Misra, P. Schiffer, R.E. Schaak, Colloidal synthesis of non-equilibrium wurtzite-type MnSe, Angew. Chemie - Int. Ed. 49 (2010) 4638–4640. https://doi.org/10.1002/anie.201001213.

[24] J. Zhang, F. Zhang, X. Zhao, X. Wang, L. Yin, C. Liang, M. Wang, Y. Li, J. Liu, Q. Wu, R. Che, Uniform wurtzite MnSe nanocrystals with surface-dependent magnetic behavior, Nano Res. 6 (2013) 275–285. https://doi.org/10.1007/s12274-013-0305-y.

[25] R.M. Murray, B.C. Forbes, R.D. Heyding, The Preparation and Paramagnetic Susceptibility of β-MnSe, Can. J. Chem. 50 (1972) 4059–4061. https://doi.org/10.1139/v72-641.

[26] J.C. Hye, Y.L. Jin, S.K. Dae, W.Y. Sang, H.K. Ja, P. Jeunghee, Morphology-tuned growth of α-MnSe one-dimensional nanostructures, J. Phys. Chem. C. 111 (2007) 519–525. https://doi.org/10.1021/jp0658187.

[27] T. Qin, J. Lu, S. Wei, P. Qi, Y. Peng, … Z.Y.-I.C., U. 2002, α-MnSe crystallites through solvothermal reaction in ethylenediamine, Elsevier. (n.d.). https://www.sciencedirect.com/science/article/pii/S1387700302003878 (toegang verkry 01 Augustus 2023).

[28] R. Masrour, E.K. Hlil, M. Hamedoun, A. Benyoussef, O. Mounkachi, H. El Moussaoui, Ab Initio, Mean Field and Series Expansions Calculations Study of Structural, Electronic and Magnetic Properties of MnAs, J. Supercond. Nov. Magn. 27 (2014) 2747–2750. https://doi.org/10.1007/s10948-014-2638-5.

[29] A. Malinauskas, Electrocatalysis at conducting polymers, Synth. Met. 107 (1999) 75–83. https://doi.org/10.1016/S0379-6779(99)00170-8.

[30] Y. Huang, H. Li, Z. Wang, M. Zhu, Z. Pei, Q. Xue, Y. Huang, C. Zhi, Nanostructured Polypyrrole as a flexible electrode material of supercapacitor, Nano Energy. 22 (2016) 422–438. https://doi.org/10.1016/j.nanoen.2016.02.047.

[31] F.F. Alharbi, H.M.T. Farid, A Nanosized Manganese-Based Chalcogenide Composite for Enhanced Electrocatalytic OER, J. Electron. Mater. 52 (2023) 3661–3671. https://doi.org/10.1007/s11664-023-10330-z.

[32] G.A. Tigwere, M.D. Khan, L.D. Nyamen, F.M. de Souza, W. Lin, R.K. Gupta, N. Revaprasadu, P.T. Ndifon, Transition metal (Ni, Cu and Fe) doped MnS nanostructures: Effect of doping on supercapacitance and water splitting, Mater. Sci. Semicond. Process. 158 (2023) 107365. https://doi.org/10.1016/j.mssp.2023.107365.

[33] H. Wang, Y. Yang, J. Liu, H. Wu, K. Wu, C. Lyu, J. Wu, W.M. Lau, Q. Wu, J. Zheng, The role of manganese-based catalyst in electrocatalytic water splitting: Recent research and progress, Mater. Today Phys. 36 (2023) 101169. https://doi.org/10.1016/j.mtphys.2023.101169.

[34] K. Kawashima, R.A. Márquez, Y.J. Son, C. Guo, R.R. Vaidyula, L.A. Smith, C.E. Chukwuneke, C.B. Mullins, Accurate Potentials of Hg/HgO Electrodes: Practical

Parameters for Reporting Alkaline Water Electrolysis Overpotentials, ACS Catal. 13 (2023) 1893–1898. https://doi.org/10.1021/acscatal.2c05655.

[35] J.L.H. Chau, M.K. Hsu, C.C. Kao, Microwave plasma synthesis of Co and SiC-coated Co nanopowders, Mater. Lett. 60 (2006) 947–951. https://doi.org/10.1016/j.matlet.2005.10.054.

[36] R.N. Singh, J.P. Pandey, N.K. Singh, B. Lal, P. Chartier, J.F. Koenig, Sol-gel derived spinel MxCo3-xO4 (M = Ni, Cu; 0≤x≤1) films and oxygen evolution, Electrochim. Acta. 45 (2000) 1911–1919. https://doi.org/10.1016/S0013-4686(99)00413-2.

[37] R.N. Singh, J.P. Singh, B. Lal, M.J.K. Thomas, S. Bera, New NiFe2-xCrxO4 spinel films for O2 evolution in alkaline solutions, Electrochim. Acta. 51 (2006) 5515–5523. https://doi.org/10.1016/j.electacta.2006.02.028.

[38] M. Wu, Y. Xiong, N. Jiang, M. Ning, Q. Chen, Hydrothermal preparation of α-MnSe and MnSe2 nanorods, J. Cryst. Growth. 262 (2004) 567–571. https://doi.org/10.1016/j.jcrysgro.2003.10.065.

[39] R. Bissessur, P.K.Y. Liu, S.F. Scully, Intercalation of polypyrrole into graphite oxide, Synth. Met. 156 (2006) 1023–1027. https://doi.org/10.1016/j.synthmet.2006.06.024.

[40] V. Abhilash, N. Rajender, K. Suresh, X-ray diffraction spectroscopy of polymer nanocomposites, in: Spectrosc. Polym. Nanocomposites, Elsevier Inc., 2016: bll 410–451. https://doi.org/10.1016/B978-0-323-40183-8.00014-8.

[41] J. Jiang, R. Yu, J. Zhu, R. Yi, G. Qiu, Y. He, X. Liu, Shape-controlled synthesis and properties of manganese sulfide microcrystals via a biomolecule-assisted hydrothermal process, Mater. Chem. Phys. 115 (2009) 502–506. https://doi.org/10.1016/J.MATCHEMPHYS.2009.01.012.

[42] J. Jiang, R. Yu, J. Zhu, R. Yi, G. Qiu, Y. He, X. Liu, Hierarchical-like multipod γ-MnS microcrystals: Solvothermal synthesis, characterization and growth mechanism, Mater. Chem. Phys. 115 (2009) 502–506. https://doi.org/10.1039/c4ra16038j.

[43] J. Yang, C. Wang, H. Ju, Y. Sun, S. Xing, J. Zhu, Q. Yang, Integrated Quasiplane Heteronanostructures of MoSe2/Bi2Se3 Hexagonal Nanosheets: Synergetic Electrocatalytic Water Splitting and Enhanced Supercapacitor Performance, Adv. Funct. Mater. 27 (2017). https://doi.org/10.1002/adfm.201703864.

[44] H.A. Alburaih, M.Z. Ansari, A.G. Abid, R.Y. Khosa, M.N. Ashiq, S. Manzoor, S. Aman, H. Chaudhry, M.S. Waheed, T.A. Taha, Study on active sites of Mn-doped iron selenide on pencil electrode for electrocatalytic water splitting, J. Sol-Gel Sci. Technol. 106 (2023) 1–9. https://doi.org/10.1007/s10971-022-05961-3.

[45] X. Zhao, X. Li, Y. Yan, Y. Xing, S. Lu, L. Zhao, S. Zhou, Z. Peng, J. Zeng, Electrical and structural engineering of cobalt selenide nanosheets by Mn modulation for efficient oxygen evolution, Appl. Catal. B Environ. 236 (2018) 569–575. https://doi.org/10.1016/j.apcatb.2018.05.054.

[46] B. Sun, G. Dong, J. Ye, D. feng Chai, X. Yang, S. Fu, M. Zhao, W. Zhang, J. Li, Selenium anion substitution endows manganese sulfide as a bifunctional electrocatalyst for efficient water splitting in alkaline solutions, Chem. Eng. J. 459 (2023) 141610. https://doi.org/10.1016/j.cej.2023.141610.

[47] Y. Zhang, J. Fu, H. Zhao, R. Jiang, F. Tian, R. Zhang, Tremella-like Ni3S2/MnS with ultrathin nanosheets and abundant oxygen vacancies directly used for high speed overall water splitting, Appl. Catal. B Environ. 257 (2019) 117899. https://doi.org/10.1016/j.apcatb.2019.117899.

[48] R.B. Pujari, G.S. Gund, S.J. Patil, H.S. Park, D.W. Lee, Anion-exchange phase control of manganese sulfide for oxygen evolution reaction, J. Mater. Chem. A. 8 (2020) 3901–3909. https://doi.org/10.1039/c9ta10553k.

[49] S. Manzoor, S. V. Trukhanov, M.N. Ansari, M. Abdullah, A. Alruwaili, A. V. Trukhanov, M.U. Khandaker, A.M. Idris, K.S. El-Nasser, T.A. Taha, Flowery ln2MnSe4 Novel Electrocatalyst Developed via Anion Exchange Strategy for Efficient Water Splitting, Nanomaterials. 12 (2022) 2209. https://doi.org/10.3390/nano12132209.

[50] H. Singh, M. Marley-Hines, S. Chakravarty, M. Nath, Multi-walled carbon nanotube supported manganese selenide as a highly active bifunctional OER and ORR electrocatalyst, J. Mater. Chem. A. 10 (2022) 6772–6784. https://doi.org/10.1039/d1ta09864k.

[51] M. Sun, R.T. Gao, X. Liu, R. Gao, L. Wang, Manganese-based oxygen evolution catalysts boosting stable solar-driven water splitting: MnSe as an intermetallic phase, J. Mater. Chem. A. 8 (2020) 25298–25305. https://doi.org/10.1039/d0ta09946e.

[52] G. Mei, H. Liang, B. Wei, H. Shi, F. Ming, X. Xu, Z. Wang, Bimetallic MnCo selenide yolk shell structures for efficient overall water splitting, Electrochim. Acta. 290 (2018) 82–89. https://doi.org/10.1016/j.electacta.2018.09.062.

[53] M. Fiaz, M. Athar, Facile Room-Temperature In Situ Incorporation of Transition-Metal Selenide (TMSe) Nanoparticles into MOF-5 for Oxygen Evolution Reaction, JOM. 72 (2020) 2219–2225. https://doi.org/10.1007/s11837-019-03867-0.

[54] X. Wei, Y. Xie, M. Liu, J. Zhou, A. Zhou, P. He, Y. Dou, J.R. Li, Multimetallic metal-organic frameworks derived transition metal doped iron selenide arrays for efficient oxygen evolution reaction, APL Mater. 7 (2019). https://doi.org/10.1063/1.5119858.

[55] A.S. Chaddha, N.K. Singh, M. Malviya, A. Sharma, Birnessite-clay mineral couple in the rock varnish: a nature's electrocatalyst, Sustain. Energy Fuels. 6 (2022) 2553–2569. https://doi.org/10.1039/d2se00185c.

[56] S. Pal, U.P. Azad, A.K. Singh, D. Kumar, R. Prakash, Studies on some spinel oxides based electrocatalysts for oxygen evolution and capacitive applications, Electrochim. Acta. 320 (2019) 134584. https://doi.org/10.1016/j.electacta.2019.134584.

[57] A. Hojatshamami, Ni-Co and Ni-Fe Catalysts for The Oxygen Evolution Reaction in Alkaline Water Electrolysis, (2022). https://hdl.handle.net/11250/3042808 (toegang verkry 23 Junie 2024).

[58] H. Zeng, Y. Zeng, J. Qi, L. Gu, E. Hong, R. Si, C. Yang, The role of proton dynamics on the catalyst-electrolyte interface in the oxygen evolution reaction, Chinese J. Catal. 43 (2022) 139–147. https://doi.org/10.1016/S1872-2067(21)63909-8.

[59] U.J. Awan, M.A. Basit, S.I.A. Shah, J. Yong-Xin, H. Zhifu, Minimized OER overpotential via SILAR-based development of g-C3N4/CdS nanocomposite, Appl. Phys. A Mater. Sci. Process. 129 (2023) 1–15. https://doi.org/10.1007/s00339-023-07105-y.

[60] Z. Hu, L. Hao, F. Quan, R. Guo, Recent developments of Co3O4-based materials as catalysts for the oxygen evolution reaction, Catal. Sci. Technol. 12 (2022) 436–461. https://doi.org/10.1039/d1cy01688a.

[61] R.L. Doyle, M.E.G. Lyons, An electrochemical impedance study of the oxygen evolution reaction at hydrous iron oxide in base, Phys. Chem. Chem. Phys. 15 (2013) 5224–5237. https://doi.org/10.1039/c3cp43464h.

[62] A. Bard, L. Faulkner, H. White, Electrochemical methods: fundamentals and applications, 2022. https://books.google.com/books?hl=en&lr=&id=Sct6EAAAQBAJ&oi=fnd&pg=PR21&ots=QV3mtaJ0NX&sig=DLfrR_jFcE_cWnGqn5_EbKOHFu0 (toegang verkry 06 Mei 2024).

[63] B.A. Mei, J. Lau, T. Lin, S.H. Tolbert, B.S. Dunn, L. Pilon, Physical Interpretations of Electrochemical Impedance Spectroscopy of Redox Active Electrodes for Electrical Energy Storage, J. Phys. Chem. C. 122 (2018) 24499–24511. https://doi.org/10.1021/acs.jpcc.8b05241.

[64] P. Leuaa, D. Priyadarshani, D. Choudhury, R. Maurya, M. Neergat, Resolving charge-transfer and mass-transfer processes of VO2+/VO2+redox species across the electrode/electrolyte interface using electrochemical impedance spectroscopy for vanadium redox flow battery, RSC Adv. 10 (2020) 30887–30895. https://doi.org/10.1039/d0ra05224h.

[65] Multiple Time Constants :: Lithium Inventory, (n.d.). https://lithiuminventory.com/experimental-electrochemistry/eis/multiple-time-constants/ (toegang verkry 26 Julie 2024).

[66] W. Mahfoz, M. Abdul Aziz, S. Shaheen Shah, A.R. Al-Betar, Enhanced Oxygen Evolution via Electrochemical Water Oxidation using Conducting Polymer and Nanoparticle Composites, Chem. - An Asian J. 15 (2020) 4358–4367. https://doi.org/10.1002/asia.202001163.

[67] W. Choi, H.C. Shin, J.M. Kim, J.Y. Choi, W.S. Yoon, Modeling and applications of electrochemical impedance spectroscopy (Eis) for lithium-ion batteries, J.

Electrochem. Sci. Technol. 11 (2020) 1–13. https://doi.org/10.33961/jecst.2019.00528.

[68] L. Wang, D. Snihirova, M. Deng, B. Vaghefinazari, D. Höche, S. V. Lamaka, M.L. Zheludkevich, Revealing physical interpretation of time constants in electrochemical impedance spectra of Mg via Tribo-EIS measurements, Electrochim. Acta. 404 (2022) 139582. https://doi.org/10.1016/j.electacta.2021.139582.

[69] B.A. Mei, J. Lau, T. Lin, S.H. Tolbert, B.S. Dunn, L. Pilon, Physical Interpretations of Electrochemical Impedance Spectroscopy of Redox Active Electrodes for Electrical Energy Storage, J. Phys. Chem. C. 122 (2018) 24499–24511. https://doi.org/10.1021/acs.jpcc.8b05241.

[70] P. Leuaa, D. Priyadarshani, D. Choudhury, R. Maurya, M. Neergat, Resolving charge-transfer and mass-transfer processes of VO2+/VO2+redox species across the electrode/electrolyte interface using electrochemical impedance spectroscopy for vanadium redox flow battery, RSC Adv. 10 (2020) 30887–30895. https://doi.org/10.1039/d0ra05224h.

[71] W. Choi, H.C. Shin, J.M. Kim, J.Y. Choi, W.S. Yoon, Modeling and applications of electrochemical impedance spectroscopy (Eis) for lithium-ion batteries, J. Electrochem. Sci. Technol. 11 (2020) 1–13. https://doi.org/10.33961/jecst.2019.00528.

[72] L. Wang, D. Snihirova, M. Deng, C. Wang, B. Vaghefinazari, G. Wiese, M. Langridge, D. Höche, S. V. Lamaka, M.L. Zheludkevich, Insight into physical interpretation of high frequency time constant in electrochemical impedance spectra of Mg, Corros. Sci. 187 (2021) 109501. https://doi.org/10.1016/j.corsci.2021.109501.

[73] H. Ai, L. Fan, Y. Wang, Z. Wang, H. Zhang, J. Zhao, M. Jiao, B. Lv, X. Han, OER catalytic performance of a composite catalyst comprising multi-layer thin flake Co3O4 and PPy nanofibers, RSC Adv. 13 (2023) 32045–32053. https://doi.org/10.1039/d3ra05936g.

[74] J. He, Z. Hu, K. Deng, R. Zhao, X. Lv, W. Tian, Y.X. Zhang, J. Ji, A triple-layered PPy@NiCo LDH/FeCo2O4hybrid crystalline structure with high electron conductivity and abundant interfaces for supercapacitors and oxygen evolution, CrystEngComm. 23 (2021) 2262–2268. https://doi.org/10.1039/d1ce00076d.

[75] R.N. Singh, N.K. Singh, J.P. Singh, Electrocatalytic properties of new active ternary ferrite film anodes for O2 evolution in alkaline medium, Electrochim. Acta. 47 (2002) 3873–3879. https://doi.org/10.1016/S0013-4686(02)00354-7.

[76] F. Švegl, B. Orel, I. Grabec-Švegl, V. Kaučič, Characterization of spinel Co3O4 and Li-doped Co3O4 thin film electrocatalysts prepared by the sol-gel route, Electrochim. Acta. 45 (2000) 4359–4371. https://doi.org/10.1016/S0013-4686(00)00543-0.

[77] R.N. Singh, J.F. Koenig, G. Poillerat, P. Chartier, Thin films of CO3O4 and NiCo2O4 prepared by the method of chemical spray pyrolysis for electrocatalysis. Part IV. The electrocatalysis of oxygen reduction, J. Electroanal. Chem. 314 (1991) 241–257. https://doi.org/10.1016/0022-0728(91)85440-Z.

[78] L.I. Krishtalik, Kinetics and mechanism of anodic chlorine and oxygen evolution reactions on transition metal oxide electrodes, Electrochim. Acta. 26 (1981) 329–337. https://doi.org/10.1016/0013-4686(81)85019-0.

[79] J.O.M. Bockris, T. Otagawa, Mechanism of oxygen evolution on perovskites, J. Phys. Chem. 87 (1983) 2960–2971. https://doi.org/10.1021/j100238a048.

[80] R.N. Singh, J.F. Koenig, G. Poillerat, P. Chartier, Thin films of CO3O4 and NiCo2O4 prepared by the method of chemical spray pyrolysis for electrocatalysis. Part IV. The electrocatalysis of oxygen reduction, J. Electroanal. Chem. 314 (1991) 241–257. https://doi.org/10.1016/0022-0728(91)85440-Z.

[81] S. Pal, U.P. Azad, A.K. Singh, D. Kumar, R. Prakash, Studies on some spinel oxides based electrocatalysts for oxygen evolution and capacitive applications, Electrochim. Acta. 320 (2019). https://doi.org/10.1016/j.electacta.2019.134584.

[82] I.H. Kwak, H.S. Im, D.M. Jang, Y.W. Kim, K. Park, Y.R. Lim, E.H. Cha, J. Park, CoSe2 and NiSe2 Nanocrystals as Superior Bifunctional Catalysts for Electrochemical and Photoelectrochemical Water Splitting, ACS Appl. Mater. Interfaces. 8 (2016) 5327–5334. https://doi.org/10.1021/acsami.5b12093.

[83] A. Bard, L. Faulkner, H. White, Electrochemical methods: fundamentals and applications, 2022. https://books.google.com/books?hl=en&lr=&id=Sct6EAAAQBAJ&oi=fnd&pg=PR21&ots=QV3mtaJ2QS&sig=WpR4J4YmgS8Ty7LGdhYY4R8tPNI (toegang verkry 06 Mei 2024).

[84] K.S. Bhat, H.S. Nagaraja, Nickel selenide nanostructures as an electrocatalyst for hydrogen evolution reaction, Int. J. Hydrogen Energy. 43 (2018) 19851–19863. https://doi.org/10.1016/j.ijhydene.2018.09.018.

[85] L. Duan, F. Bozoglian, S. Mandal, B. Stewart, T. Privalov, A. Llobet, L. Sun, A molecular ruthenium catalyst with water-oxidation activity comparable to that of photosystem II, Nat. Chem. 4 (2012) 418–423. https://doi.org/10.1038/nchem.1301.

[86] J.J. Concepcion, M.K. Tsai, J.T. Muckerman, T.J. Meyer, Mechanism of water oxidation by single-site ruthenium complex catalysts, J. Am. Chem. Soc. 132 (2010) 1545–1557. https://doi.org/10.1021/ja904906v.

[87] S.B. Sinha, D.Y. Shopov, L.S. Sharninghausen, C.J. Stein, B.Q. Mercado, D. Balcells, T.B. Pedersen, M. Reiher, G.W. Brudvig, R.H. Crabtree, Redox Activity of Oxo-Bridged Iridium Dimers in an N,O-Donor Environment: Characterization of Remarkably Stable Ir(IV,V) Complexes, J. Am. Chem. Soc. 139 (2017) 9672–9683. https://doi.org/10.1021/jacs.7b04874.

[88] Z. Codolà, I. Gamba, F. Acuna-Parés, C. Casadevall, M. Clémancey, J.M. Latour, J.M. Luis, J. Lloret-Fillol, M. Costas, Design of Iron Coordination Complexes as Highly Active Homogenous Water Oxidation Catalysts by Deuteration of Oxidation-Sensitive Sites, J. Am. Chem. Soc. 141 (2019) 323–333. https://doi.org/10.1021/jacs.8b10211.

[89] L. Francàs, R. Matheu, E. Pastor, A. Reynal, S. Berardi, X. Sala, A. Llobet, J.R. Durrant, Kinetic Analysis of an Efficient Molecular Light-Driven Water Oxidation System, ACS Catal. 7 (2017) 5142–5150. https://doi.org/10.1021/acscatal.7b01357.

[90] C.A. Mesa, E. Pastor, L. Francàs, UV–Vis operando spectroelectrochemistry for (photo)electrocatalysis: Principles and guidelines, Curr. Opin. Electrochem. 35 (2022) 101098. https://doi.org/10.1016/j.coelec.2022.101098.

[91] Y.W. Choi, H. Mistry, B. Roldan Cuenya, New insights into working nanostructured electrocatalysts through operando spectroscopy and microscopy, Curr. Opin. Electrochem. 1 (2017) 95–103. https://doi.org/10.1016/j.coelec.2017.01.004.

[92] C.J. Jafta, A. Hilger, X.G. Sun, L. Geng, M. Li, S. Risse, I. Belharouak, I. Manke, A Multidimensional Operando Study Showing the Importance of the Electrode Macrostructure in Lithium Sulfur Batteries, ACS Appl. Energy Mater. 3 (2020) 6965–6976. https://doi.org/10.1021/acsaem.0c01027.

[93] K.J. Lee, N. Elgrishi, B. Kandemir, J.L. Dempsey, Electrochemical and spectroscopic methods for evaluating molecular electrocatalysts, Nat. Rev. Chem. 1 (2017). https://doi.org/10.1038/s41570-017-0039.

[94] B.E. Conway, P.L. Bourgault, THE ELECTROCHEMICAL BEHAVIOR OF THE NICKEL – NICKEL OXIDE ELECTRODE: PART I. KINETICS OF SELF-DISCHARGE, Can. J. Chem. 37 (1959) 292–307. https://doi.org/10.1139/V59-038.

[95] D.K. Bediako, Y. Surendranath, D.G. Nocera, Mechanistic studies of the oxygen evolution reaction mediated by a nickel-borate thin film electrocatalyst, J. Am. Chem. Soc. 135 (2013) 3662–3674. https://doi.org/10.1021/ja3126432.

[96] Y. Surendranath, M.W. Kanan, D.G. Nocera, Mechanistic studies of the oxygen evolution reaction by a cobalt-phosphate catalyst at neutral pH, J. Am. Chem. Soc. 132 (2010) 16501–16509. https://doi.org/10.1021/JA106102B.

[97] C. Costentin, D.G. Nocera, Self-healing catalysis in water, Proc. Natl. Acad. Sci. U. S. A. 114 (2017) 13380–13384. https://doi.org/10.1073/PNAS.1711836114.

[98] A. Moysiadou, S. Lee, H.C.-J. of the A. Hsu, CS, U. 2020, Mechanism of oxygen evolution catalyzed by cobalt oxyhydroxide: cobalt superoxide species as a key intermediate and dioxygen release as a rate-determining step, ACS Publ. 142 (2020) 11901–11914. https://doi.org/10.1021/jacs.0c04867.

[99] L.P. Wang, T. Van Voorhis, Direct-coupling O2 bond forming a pathway in cobalt oxide water oxidation catalysts, J. Phys. Chem. Lett. 2 (2011) 2200–2204. https://doi.org/10.1021/JZ201021N.

[100] R.R. Rao, S. Corby, A. Bucci, M. García-Tecedor, C.A. Mesa, J. Rossmeisl, S. Giménez, J. Lloret-Fillol, I.E.L. Stephens, J.R. Durrant, Spectroelectrochemical Analysis of the Water Oxidation Mechanism on Doped Nickel Oxides, J. Am. Chem. Soc. 144 (2022) 7622–7633.

https://doi.org/10.1021/JACS.1C08152/ASSET/IMAGES/LARGE/JA1C08152_0005.JPEG.

[101] H. Mashiko, K. Yoshimatsu, T. Oshima, A. Ohtomo, Fabrication and Characterization of Semiconductor Photoelectrodes with Orientation-Controlled α-Fe2O3 Thin Films, J. Phys. Chem. C. 120 (2016) 2747–2752. https://doi.org/10.1021/ACS.JPCC.5B10838.

[102] J.E. Jee, O. Pestovsky, A. Bakac, Preparation and characterization of manganese(IV) in aqueous acetic acid, Dalt. Trans. 39 (2010) 11636–11642. https://doi.org/10.1039/c0dt00476f.

[103] H. Ren, F. Yang, Influence of Mn2+ on the up-conversion emission performance of Mn2+, Yb3+, Er3+: ZnWO4 green phosphors, J. Mater. Sci. Mater. Electron. 29 (2018) 15396–15403. https://doi.org/10.1007/s10854-018-9053-9.

[104] T. Takashima, K. Hashimoto, R. Nakamura, Mechanisms of pH-dependent activity for water oxidation to molecular oxygen by MnO 2 electrocatalysts, J. Am. Chem. Soc. 134 (2012) 1519–1527. https://doi.org/10.1021/ja206511w.

[105] D. Sekiguchi, S. Adachi, Synthesis and photoluminescence spectroscopy of BaGeF6:Mn4+ red phosphor, Opt. Mater. (Amst). 42 (2015) 417–422. https://doi.org/10.1016/j.optmat.2015.01.039.

[106] R. Cao, J. Qiu, X. Yu, X. Sun, Spectroscopic Investigation on BaSO 4 :(Mn 6+ , Mn 5+) Crystal, ECS J. Solid State Sci. Technol. 2 (2013) R237–R240. https://doi.org/10.1149/2.020311jss.

[107] C.C. Perry, X. Li, Structural studies of gel phases. Part 2. - Infrared spectroscopic study of silica monoliths; The interaction of water with surface species, J. Chem. Soc. Faraday Trans. 87 (1991) 3857–3862. https://doi.org/10.1039/FT9918703857.

[108] M. Takeuchi, G. Martra, S. Coluccia, M. Anpo, Evaluation of the adsorption states of H2O on oxide surfaces by vibrational absorption: Near- And mid-infrared spectroscopy, J. Near Infrared Spectrosc. 17 (2009) 373–384. https://doi.org/10.1255/jnirs.843.

[109] I. Roy, Q. Wang, V. Chakrapani, Nature of Reaction Intermediates and Origin of Bifunctionality in Manganese Oxide, J. Phys. Chem. C. 124 (2020) 5286–5299. https://doi.org/10.1021/acs.jpcc.0c00714.